



# A sliding-bed particle solar receiver with controlling particle flow velocity for high-temperature thermal power generation

Xiangyu Xie <sup>1</sup>, Haoran Xu <sup>1</sup>, Di Gan, Mingjiang Ni, Jianhua Yan, Kefa Cen, Gang Xiao <sup>\*</sup>

State Key Laboratory of Clean Energy Utilization, Zhejiang University, 38 Zheda Road, Hangzhou, 310029, China

## ARTICLE INFO

### Article history:

Received 10 June 2021

Received in revised form

13 October 2021

Accepted 27 October 2021

Available online 30 October 2021

### Keywords:

Solar energy

Sliding-bed particle receiver

Flow control

Structural design

## ABSTRACT

Various impeded flow particle receivers were proposed to prolong the particle residence time but always faced the risk of thermal deterioration and the difficulty of real-time particle velocity control. Herein, we reported a novel impeded flow particle receiver to solve above problems and further have the potential to control the particle velocity distribution, which could provide a heat source with better stability, better uniformity and higher temperature for subsequent thermal power generation and other thermal applications. In this receiver, the friction along the path and the gate valves at outlet act as the obstruction structures to allow the particles to move slowly and controllably in the form of a sliding-bed, which is why we call this receiver a sliding-bed receiver. The sliding-bed receiver's structural validity and operational characteristics at different working conditions were detailedly investigated with both experimental and numerical methods. Experimental results showed that the outlet particle temperature and efficiency could reach 847 °C and 77.2% under a solar simulator of 4 kW. An optical and thermal coupling model was developed and revealed an improved particle temperature of 1350 °C and efficiency of 82% under higher incident power. The effects of the effects of the incident power distribution, the particle velocity distribution and the quartz glass on aperture on the receiver performance were detailedly analyzed, which could also help optimize the design and operation of other particle receivers such as free-falling particle receivers.

© 2021 Elsevier Ltd. All rights reserved.

## 1. Introduction

The growing concerns on global warming and related environmental problems require significant efforts on the utilization of renewable energies. Solar energy is clean, abundant, sustainable and available all over the world. Its efficient and cost-effective utilization is a key to the long-term prosperity of human society. Solar receivers can convert solar energy into heat energy to facilitate subsequent applications. The characteristics of the solar receivers are largely affected by the types of heat transfer media. Compared with molten salt, particles can benefit from its high heat-resistance [1,2] and low price [4,5]. Besides, there are no piping problems such as freezing [6]. The high-temperature particles can serve as a heat source of supercritical CO<sub>2</sub> cycle, as well as hydrogen production or coal gasification [7].

The concept of free-falling particle receivers was first proposed by Hruby et al., in 1986 [8]. Ho et al. developed this structure and conducted on-sun tests which achieved an outlet temperature of 700 °C by recirculated heating [9,10]. The free-falling particle receivers had a relatively simple structure and stable operation, but suffered from an insufficient single-pass temperature rise due to the high velocity (i.e. short residence time) of particles. To reduce the particle velocity, the impeded flow particle receivers were proposed. Ho et al. further proposed and tested the  $\Delta$ -plate type impeded flow particle receivers, and they managed to increase the particle temperature rise from 100 to 150 °C/m (600 kW/m<sup>2</sup>) to 200 °C/m (400 kW/m<sup>2</sup>) [11]. However, the  $\Delta$ -plates which acted as obstructed structures were at risk of deterioration due to the direct heating by the incident power. Other impeded flow particle receivers such as using the porous ceramic foam structures by Lee et al. [12] and horizontal wire mesh screens by Sandlin et al. [13,14] as the obstructed structures were also proposed, but still faced the same problem as  $\Delta$ -plate type receivers and needed further on-sun tests to verify their operation stability. Compared with the constant endothermic process for the basic form of free-falling and impeded

<sup>\*</sup> Corresponding author.

E-mail address: [xiaogantianmen@zju.edu.cn](mailto:xiaogantianmen@zju.edu.cn) (G. Xiao).

<sup>1</sup> These authors contributed equally to this paper.

Nomenclature (international system of units)			
$Q$	net power or heat transfer power	$\sigma$	Stefan-Boltzmann constant
$Q_{flow}$	heat transfer due to particle flow	$g$	gravity coefficient
$T$	temperature	$\varphi$	loss rate
$T_m$	characteristic temperature	$\eta$	efficiency
$\dot{m}$	particle mass flow rate for one control volume	<i>Subscripts</i>	
$\dot{m}_{sum}$	total particle mass flow rate	<i>inlet</i>	inlet of the receiver
$\tau$	time step	<i>end</i>	end of the inclined plate
$t_{valid}$	valid heat transfer time	<i>outlet</i>	outlet of the receiver
$A$	area	<i>incline</i>	inclined plate
$A_{valid}$	valid heat transfer area	<i>funnel</i>	connecting funnel
$d$	layer or interlayer thickness	$g$	quartz glass
$l$	characteristic length	$p$	particles
$\theta$	tilt angle of the inclined plate	$fp$	flowing particles
$c$	specific heat	$sp$	stagnant particles
$\rho$	bulk density	$rad$	radiation (heat transfer)
$\nu$	kinematic viscosity coefficient	$conv$	convection (heat transfer)
$\lambda$	thermal conductivity	$cond$	conduction (heat transfer)
$h$	convection coefficient	$opt$	optical property
$\epsilon$	emissivity	$ther$	thermal property
$r$	reflectivity	$total$	total property
$Pr$	Prandtl number	$ave$	average property
$Gr$	Grashof number	$pre$	previous property

flow particle receivers, the real-time control of particle was further needed to meet the varied incident power. Therefore, a free-falling particle receiver with an automated slide gate implemented at the top hopper was tested, which could control the particle mass flow into the receiver and thus the outlet temperature [15], but the particle velocity was not substantially controlled and the deficiency of single-pass temperature rise still existed. In addition, the centrifugal particle receivers by Wu et al. [16–18] and the spiral particle receivers by Xiao et al. [7,19] were also proposed and had the ability to control particle velocity by adjusting the rotating speed and vibration frequency respectively, but they both needed additional power and had moving parts such as rotating and electromagnetic vibration structures respectively, which might pose a threat to the stable operation at high temperatures. Besides the control of the overall velocity of particles, it is also noteworthy to control the velocity distribution of particles to match the non-uniformity of incident power, which always has stronger intensity in the middle and weaker intensity in the edge, but there is still a lack of attention and corresponding structural design in this regard.

Herein, a novel impeded flow particle receiver was proposed and tested, trying to alleviate the deterioration risk and achieve the real-time particle velocity control and even velocity distribution control, which could provide a more stable, more uniform and higher-temperature heat source for applications. In this receiver, the inclined plate is used as the radiation absorption area, and the outlet valves are used to control the particle flow rate and thus control the particle velocity. The friction along the path and the gate valves at outlet act as the obstruction structures, which allow the particles to move slowly and controllably in the form of a sliding bed, which is why we call this receiver a sliding-bed receiver. Furthermore, the velocity distribution control has the potential to be achieved by setting multiple connecting funnels and electric gate valves in the transverse direction. The sliding-bed receiver's structural validity and operational characteristics at different working conditions were detailedly investigated with both experimental and numerical methods. The performance of the sliding-bed receiver in practical applications such as the dish-type

and the tower-type concentrated solar power systems were further forecasted. The effects of the effects of the incident power distribution, the particle velocity distribution and the quartz glass on aperture on the performance of this receiver were detailedly analyzed, which could also help optimize the design and operation of this receiver and other particle receivers such as free-falling particle receivers.

## 2. Receiver design

The working particle selected was sintered bauxite, whose optical and thermodynamic properties met the operation requirements of sliding-bed particle receiver and the details were listed in Table 1.

As shown in Fig. 1, the sliding-bed particle receiver tested in laboratory was mainly composed of an up silo, an inclined plate, a connecting funnel with internal obstructed structure, and an electric gate valve. The length and width of the inclined plate were 1000 and 350 mm, respectively. The whole body of the sliding-bed receiver was made of 310 S stainless steel, which could withstand 1400 °C without melting, and aluminum silicate was used as the insulation material. The particles inside the up silo came out through a slit and were transported along the inclined plate by

**Table 1**  
Properties of particles.

Properties	Item
Composition	83%-Al <sub>2</sub> O <sub>3</sub> , 5%-SiO <sub>2</sub> , 6%-Fe <sub>2</sub> O <sub>3</sub> and others
Size (mm)	0.5–0.8 (0.712 in average)
Absorptivity	85%
Heat capacity (J kg <sup>-3</sup> K <sup>-1</sup> )	756 (25 °C) ~ 1275 (700 °C)
Bulk density (kg m <sup>-3</sup> )	1800
Density (kg m <sup>-3</sup> )	2650
Packing limit	0.68
Angle of repose (°)	23
Thermal conductivity (W m <sup>-1</sup> K <sup>-1</sup> )	0.23 (20 °C) ~ 0.54 (800 °C)
Price (\$/ton)	760

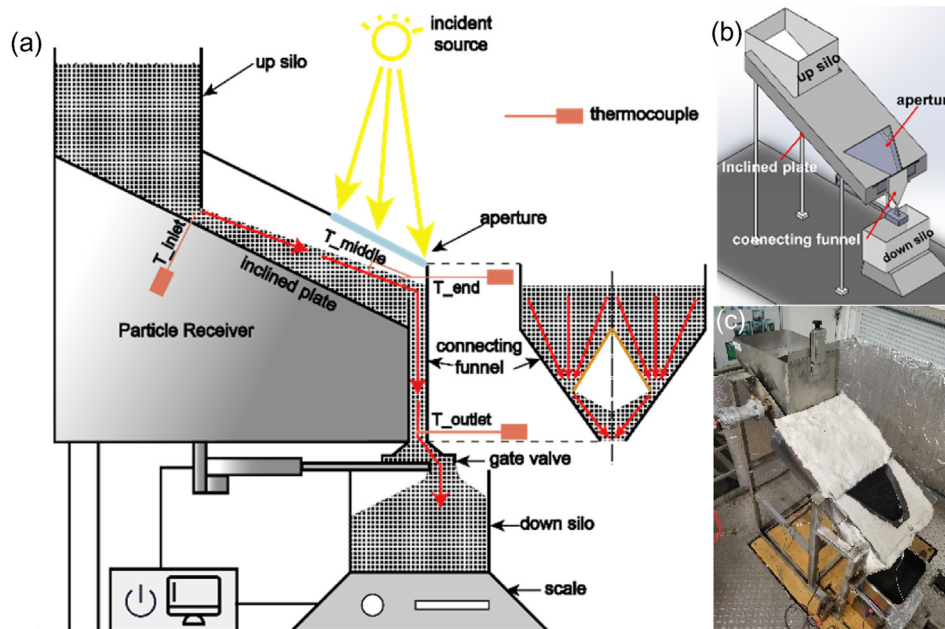


Fig. 1. (a) The schematic, (b) the configuration and (c) the experimental setup of the sliding-bed particle receiver.

gravity, where they were directly heated by the concentrated radiation. Then the particles slid into the connecting funnel and entered the down silo through an electric gate valve. The electric gate valve could control the particle flow rate and thus control the particle velocity on inclined plate. A quartz glass was attached on the aperture for sealing purpose, and could reduce the heat loss with greenhouse effect at the same time. During the whole operation, the particles moved in the form of a sliding bed inside the receiver.

To ensure a smooth particle flow, the angle of the inclined plate was selected to be  $2\text{--}5^\circ$  larger than the angle of repose, resulting in an increase in the particle layer thickness along the downstream as shown in Fig. 2(a). To avoid the particles at the bottom of particle layer that have relatively cold temperatures to leave the inclined plate, an adjustable baffle was added to the end of the inclined plate as shown in Fig. 2(b). In this way, the higher outlet temperature of the sliding-bed receiver could be achieved as only the surface particles with a higher temperature could leave the inclined plate. Because the inclined plate was always covered with particles (especially the stagnant particles which couldn't cross the end baffle) and other internal parts of the receiver were not exposed to direct radiation either, the risk of thermal deterioration was significantly alleviated.

Connecting funnel was an important sector between the inclined plate and receiver outlet, as they could concentrate the particle flow from the wide plate end to the narrow valve opening. For the simplest form of connecting funnel as Fig. 2(c), the maximum particle velocity occurred in the direction right towards the funnel outlet, which always led to an unwanted velocity distribution on inclined plate. To alleviate this problem, two kinds of obstructed structures inside the funnel were designed as shown in Fig. 2(d)–(e). Through the test of models made of polymethacrylate, these two structures were both found to be effective. Considering the manufacturing difficulty and cost-effective, the obstructed structure as shown in Fig. 2(d) was finally adopted in the current experimental setup.

As shown in Fig. 3(a), the flow rate and temperature control system is composed by the following parts, i.e. the electric gate valve, the electronic scale, the particle storage bin and the

thermocouples. The thermocouples were placed along the inclined plate and the connecting funnel for real-time particle temperature measurement. When the measured outlet temperature was below the required value, the electric pusher moved forward to decline the gate valve opening and reduce the particle flow rate. In this way, the particle velocity was reduced and thus the outlet temperature was increased, and vice versa. The receiver efficiency was calculated and recorded in real time based on the mass of particles flowing into the particle storage bin, the incident power and the particle temperatures at inlet and outlet of the receiver. To reduce jamming caused by high operating temperature, a large space (30 cm) was kept between the motor and the valve as shown in Fig. 3(a).

At present, only one connecting funnel and one electric gate valve were set and tested in hot state due to the low incident power of solar simulator and therefore the small size of the receiver. But there is potential for velocity distribution control by setting multiple connecting funnels and electric gate valves in the transverse direction, which has been preliminarily tested in cold state on a larger sliding-bed receiver as shown in Fig. 3(b), and further hot-state tests still await the manufacturing and arrangement of a heliostat field with  $\sim 500$  kW incident power.

### 3. Model

For a better understanding of the current experimental results and a prediction of the receiver performance under higher incident conditions such as dish-type and the tower-type concentrated solar power systems, an optical-thermal coupled model discretizing the heat transfer process in time and space was proposed. The heat transfer process of the particles mainly takes place in the inclined plate section and the connecting funnel section.

#### 3.1. Inclined plate section

##### 3.1.1. Model assumptions

To simplify the model while keeping a high accuracy, following assumptions are adopted:

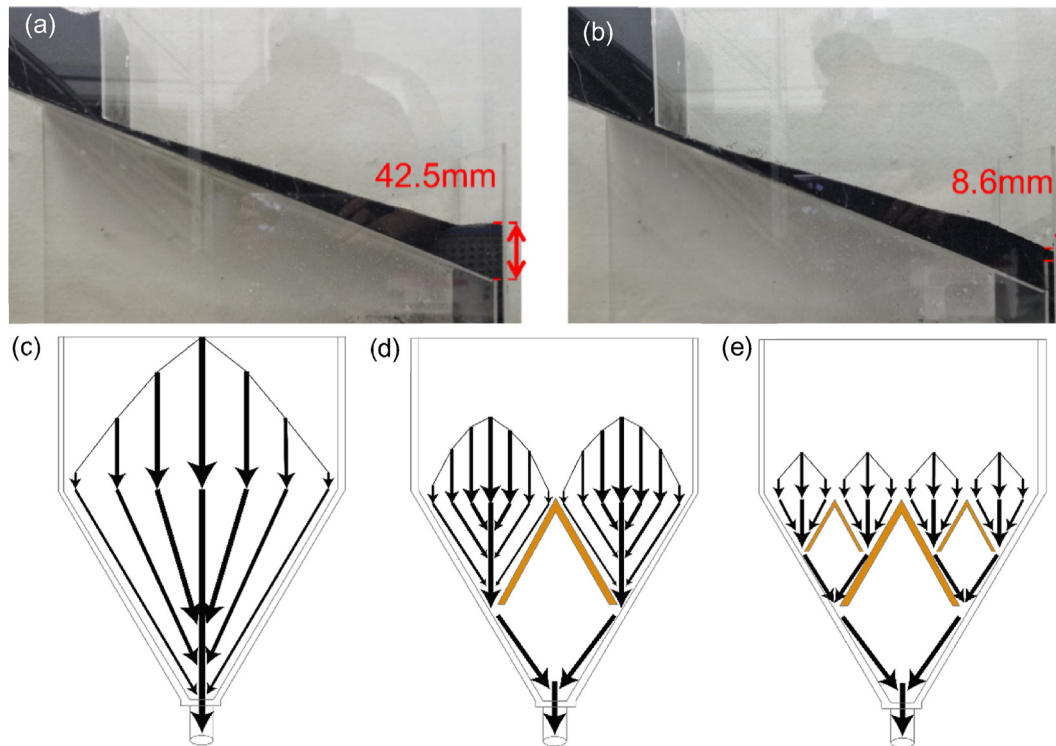


Fig. 2. The states of particle layer (a) without end baffle and (b) with end baffle, and the qualitative particle flow distributions inside the funnel (c) without, (d) with simple, and (e) with complicated obstructed structures.

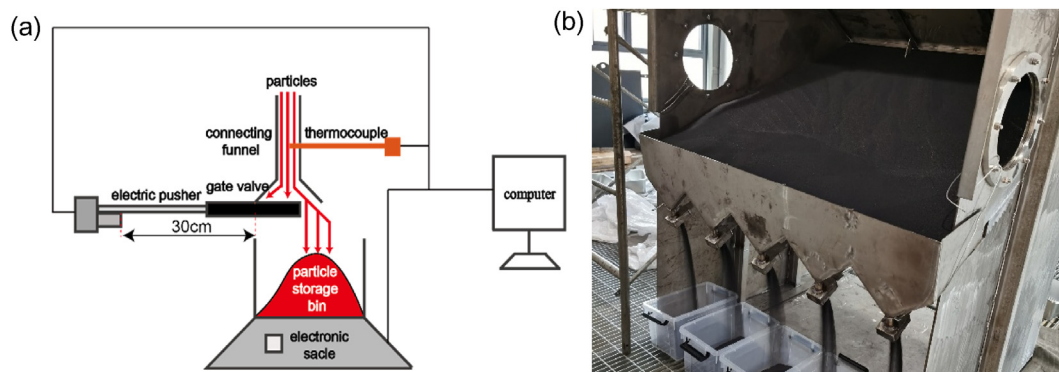


Fig. 3. (a) Schematic of the mass-flow and temperature control system and (b) cold-state test of particle velocity distribution control by setting multiple connecting funnels and electric gate valves.

- a) The ambient temperature is considered to be constant as the laboratory is equipped with constant temperature air conditioning.
- b) The temperature of particles at the inlet is the same as the ambient temperature as the particles inside the up silo are all fully cooled at ambient temperature.
- c) The incident power of each grid was measured by a CCD-camera Lambertian method as mentioned above.
- d) All sidewalls and the inclined plate under the stagnant particle layer are regarded as isothermal as an adequate thermal insulation treatment was added.
- e) The surface of particle layer is assumed to be continuous and only exchanges heat with the quartz glass facing it due to the close proximity (45 mm) between particles and quartz glass.
- f) The whole particle lay is divided into flowing particle layer and stagnant particle layer due to end baffle and the thickness of flowing particle layer is measured to be about 11 mm.

### 3.1.2. Governing equations

The schematic of the heat transfer model for the inclined plate section is shown in Fig. 4. For the real-time power change of each grid, the radiation heat transfer calculated by Monte Carlo method and the non-negligible convection and conduction heat transfers calculated by empirical formula with surrounding objects are considered, and the heat transfer caused by the incoming and outgoing particles of each grid should also be considered for the flowing particles. Therefore, the energy equations for the quartz

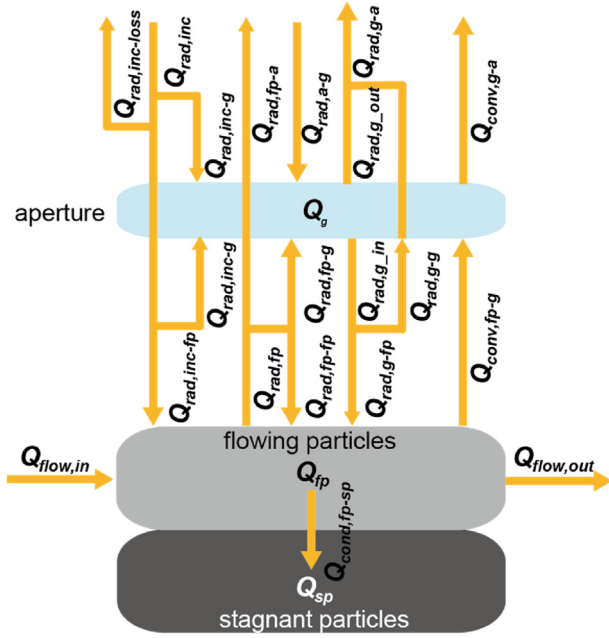


Fig. 4. Schematic of the heat transfer model for the inclined plate section.

glass, flowing particle layer and stagnant particle layer can be expressed as given in Eqs. (1)–(3).

$$Q_g = Q_{rad,inc-g} + Q_{rad,g\_mutual} + Q_{conv,g\_mutual} \quad (1)$$

$$Q_{fp} = Q_{flow} + Q_{rad,inc-fp} + Q_{rad,fp\_mutual} + Q_{conv,fp\_mutual} - Q_{cond,fp-sp} \quad (2)$$

$$Q_{sp} = Q_{cond,fp-sp} \quad (3)$$

Here  $Q_g$ ,  $Q_{fp}$  and  $Q_{sp}$  are the net powers gained by quartz glass, flowing and stagnant particles, respectively.  $Q_{rad,inc-g}$  and  $Q_{rad,inc-fp}$  are the radiation heat transfers from incident source to quartz glass and flowing particles, respectively.  $Q_{rad,g\_mutual}$ ,  $Q_{rad,fp\_mutual}$ ,  $Q_{conv,g\_mutual}$  and  $Q_{conv,fp\_mutual}$  are the mutual radiation and convection heat transfers between quartz glass and flowing particles and others, respectively.  $Q_{cond,fp-sp}$  is the conduction heat transfer from flowing particles to stagnant particles.  $Q_{flow}$  is the heat transfer due to particle flow in and out.

Please refer to the supplementary materials for the specific calculation of the energy conservation formulas.

After obtaining the values of  $Q_g$ ,  $Q_{fp}$  and  $Q_{sp}$ , the temperature change of quartz glass, flowing particle layer and stagnant particle layer within each time step can be calculated by Eqs. (4)–(6).

$$\Delta T_g = Q_g \Delta \tau / (c_g A_g d_g \rho_g) \quad (4)$$

$$\Delta T_{fp} = Q_{fp} \Delta \tau / (c_{fp} A_{fp} d_{fp} \rho_{fp}) \quad (5)$$

$$\Delta T_{sp} = Q_{sp} \Delta \tau / (c_{sp} A_{sp} d_{sp} \rho_{sp}) \quad (6)$$

Here  $\Delta \tau$  is the time step,  $c_g$ ,  $c_{fp}$  and  $c_{sp}$  are the heat capacities,  $A_g$ ,  $A_{fp}$  and  $A_{sp}$  are the heat transfer areas,  $d_g$ ,  $d_{fp}$  and  $d_{sp}$  are the layer thicknesses, and  $\rho_g$ ,  $\rho_{fp}$  and  $\rho_{sp}$  are the bulk densities of quartz glass, flowing particles and stagnant particles respectively.

Eq. (5) gives the temperature of flowing particles in each control

volume and each time step, and then the efficiency for the inclined plate section is expressed by Eq. (7).

$$\eta_{incline} = \left( \sum c_{end} \dot{m}_{end} T_{end} - c_{inlet} \dot{m}_{sum} T_{inlet} \right) / \sum Q_{rad,inc} \quad (7)$$

Here  $c_{end}$ ,  $\dot{m}_{end}$  and  $T_{end}$  are respectively the particle heat capacity, particle mass flow rate and particle temperature of any grid at the end of the inclined plate,  $c_{inlet}$  and  $T_{inlet}$  are respectively the heat capacity and temperature of the particles at the inlet of receiver,  $\dot{m}_{sum}$  is the total particle mass flow rate which is equal to the sum of  $\dot{m}_{end}$ , and  $Q_{rad,inc}$  is the incident power of any grid on aperture.

The optical loss rate and thermal loss rate (to incident power) of the inclined plate is further expressed as Eq. (8) and Eq. (9).

$$\varphi_{incline,opt} = \sum Q_{rad,inc-loss} / \sum Q_{rad,inc} \quad (8)$$

$$\varphi_{incline,ther} = \left( (1 - \eta_{incline}) \times \sum Q_{rad,inc} - \sum Q_{rad,inc-loss} \right) / \sum Q_{rad,inc} \quad (9)$$

Here optical loss is defined as the loss due to the incident ray escape, and thermal loss is defined as the sum of convection, conduction and radiation loss from the receiver and internal particles.

### 3.2. Connecting funnel section

#### 3.2.1. Model assumptions

To simplify the model while keeping a high accuracy, following assumptions are adopted:

- The ambient temperature is considered constant as the laboratory is equipped with constant temperature air conditioning.
- Only radiation heat transfer occurs between particles and the inner wall of the connecting funnel due to the poor thermal conductivity of particles.
- The outlet particle temperature is considered uniform due to the small size of the receiver outlet.
- The heat capacity of insulation is ignored due to its low density.
- The heat capacity of the outer wall of the connecting funnel is ignored due to its thinness.
- The whole connecting funnel (without particles) is regarded as one control volume due to its low capacity.

#### 3.2.2. Governing equations

The schematic of the heat transfer model for the connecting funnel section is shown in Fig. 5.  $Q_p$  and  $Q_s$  are the net powers gained by particles and funnel's inner wall, respectively.  $Q_{rad,p-s}$  is the radiation heat transfer from particles to steel.  $Q_{cond,ins}$  is the conduction heat transfer through the insulation.  $Q_{conv,s-a}$  and

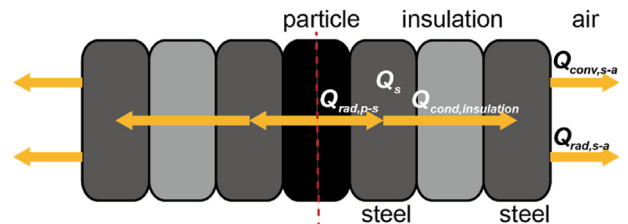


Fig. 5. Schematic of the heat transfer model for the connecting funnel section.

$Q_{rad,s-a}$  are respectively the convection and radiation heat transfers from steel to atmosphere.

The energy equation for the particles and steel can be expressed as Eq. (10) and Eq. (11).

$$Q_p = 2Q_{rad,p-s} \quad (10)$$

$$Q_s = 2Q_{rad,p-s} - 2Q_{cond,ins} \quad (11)$$

Here  $Q_{rad,p-s}$  is calculated by considering multiple reflections and absorptions as shown in Eq. (12).

$$Q_{rad,p-s} = A_{valid} \varepsilon_p \varepsilon_s \sigma \left/ (1 - r_p r_s) \right. \cdot \left( \left( T_{pre\_ave\_end} / 2 + T_{pre\_outlet} / 2 \right)^4 - T_s^4 \right) \quad (12)$$

Here  $\varepsilon_p$ ,  $\varepsilon_s$ ,  $r_p$  and  $r_s$  are the emissivity and reflectivity of particles and steel respectively,  $T_{pre\_ave\_end}$  and  $T_{pre\_outlet}$  are the previous average temperature of the particles at the end of the inclined plate and the outlet of the receiver respectively, and  $A_{valid}$  is the valid heat transfer area as calculated by Eq. (13).

$$A_{valid} = \dot{m}_{sum} \tau \left/ (\rho_p d_{funnel}) \right. \quad (13)$$

Here  $\rho_p$  is the bulk density of particles and  $d_{funnel}$  is the interlayer thickness of connecting funnel.

$Q_{cond,ins}$  conforms to the following energy equation regardless the heat capacities of insulation and the outer wall of the connecting funnel as expressed in Eq. (14).

$$Q_{cond,ins} = Q_{rad,s-a} + Q_{conv,s-a} \quad (14)$$

Here  $Q_{rad,s-a}$  and  $Q_{conv,s-a}$  are calculated in the same way as  $Q_{rad,g\_out}$  and  $Q_{conv,g-a}$ .

Therefore, the temperature of particles at the outlet of the receiver can be expressed as Eq. (15).

$$T_{outlet} = T_{ave\_end} - 2Q_{rad,p-s} t_{valid} \left/ (c_p \dot{m}_{sum} \tau) \right. \quad (15)$$

Here  $T_{ave\_end}$  and  $T_{outlet}$  are the current average temperature of the particles at the end of the inclined plate and the outlet of the receiver respectively,  $c_p$  is the heat capacity of particles and  $t_{valid}$  is the valid heat transfer time as calculated by Eq. (16).

$$t_{valid} = V_{funnel} \rho_p \left/ \dot{m}_{p\_sum} \right. \quad (16)$$

Here  $V_{funnel}$  is the volume of connecting funnel.

The efficiency for the connecting funnel section is calculated by Eq. (17).

$$\eta_{funnel} = \left( \eta_{incline} \sum Q_{rad,inc} - 2Q_{rad,p-s} \right) \left/ \left( \eta_{incline} \sum Q_{rad,inc} \right) \right. \quad (17)$$

The thermal loss rate of connecting funnel (to incident power) is calculated by Eq. (18).

$$\varphi_{funnel,ther} = 2Q_{rad,p-s} \left/ \sum Q_{rad,inc} \right. \quad (18)$$

Consequently, the optical loss rate, thermal loss rate, total loss rate and total efficiency are defined as Eq. (19) – (22),

$$\varphi_{opt} = \varphi_{incline,opt} \quad (19)$$

$$\varphi_{ther} = \varphi_{incline,ther} + \varphi_{funnel,ther} \quad (20)$$

$$\varphi_{total} = \varphi_{opt} + \varphi_{ther} \quad (21)$$

$$\eta_{total} = 1 - \varphi_{total} \quad (22)$$

Here  $\eta_{total}$  can also be expressed by Eq. (23).

$$\eta_{total} = (c_{outlet} T_{outlet} - c_{inlet} T_{inlet}) \dot{m}_{sum} \left/ \sum Q_{rad,inc} \right. \quad (23)$$

Here  $c_{ave\_outlet}$  is the average heat capacity of particles at the outlet of the receiver.

## 4. Experiments and discussions

### 4.1. Experimental conditions and results

In experiments, the valid test duration of each case was about 3000 s and the ambient temperature was about 20 °C. The incident power was provided by a solar simulator consisted of 14 individual units as shown in Fig. 6(a). The irradiance distribution on receiver aperture shown in Fig. 6(b) was measured by a CCD-camera Lambertian method [20,21] and the total radiation was about 4 kW.

The velocity distribution of surface particles as shown in Fig. 7(a) was measured by trace method, where the peak particle velocity was found to be directly opposite the slit of the obstructed instruction and the slowest particles were at the edge of flow.

As shown in Fig. 7(b), the outlet temperature curve had a turning point and the maximum outlet temperatures ( $T_{outlet}$ ) were found at about 1.5 g/s, where the cases with and without quartz glass were 847.7 and 769.4 °C respectively. While the total efficiency ( $\eta_{total}$ ) was found to continuously grow with the increase of particle flow rate, where the cases with and without quartz glass reached 77.2% and 71.9% at a flow rate of over 4.5 g/s, respectively. Both  $T_{outlet}$  and  $\eta_{total}$  with quartz glass presented higher values than those without quartz glass, indicating the greenhouse effect created by quartz glass could reduce the energy loss of the sliding-bed receiver.

Through the real-time  $T_{outlet}$  with different flow rates as shown in Fig. 7(c), it was found that  $T_{outlet}$  rose rapidly in the beginning stage, reaching more than 80% of the final stable value within 570 s, 425 s and 265 s with the flow rate of 1.49 g/s, 2.93 g/s and 3.95 g/s respectively. Obviously, with the increase of flow rate, the rate of temperature rising to a stable state became faster, which was because that the particles could transfer heat to the receiver more quickly and the high-temperature particles could move to the receiver outlet more quickly with a higher flow rate. In addition, the temperature fluctuation due to the “landslide” which could be observed in cold-state experiments was also alleviated with the increase of particle flow. The real-time record and time-dependent simulation at 2.93 g/s is presented in Fig. 7(d), where the temperature fluctuation at outlet was much smaller than that in the middle due to the buffering effect of connecting funnel.

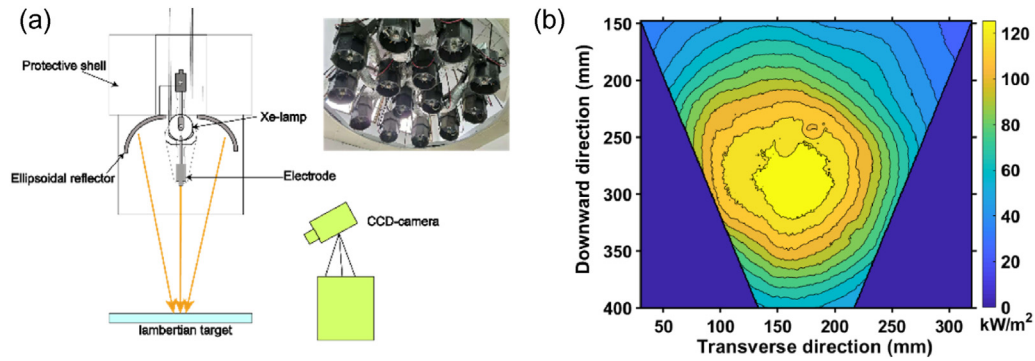


Fig. 6. (a) Configuration of a single solar simulator unit and CCD-camera Lambertian measurement method and (b) radiation distribution of the solar simulator system.

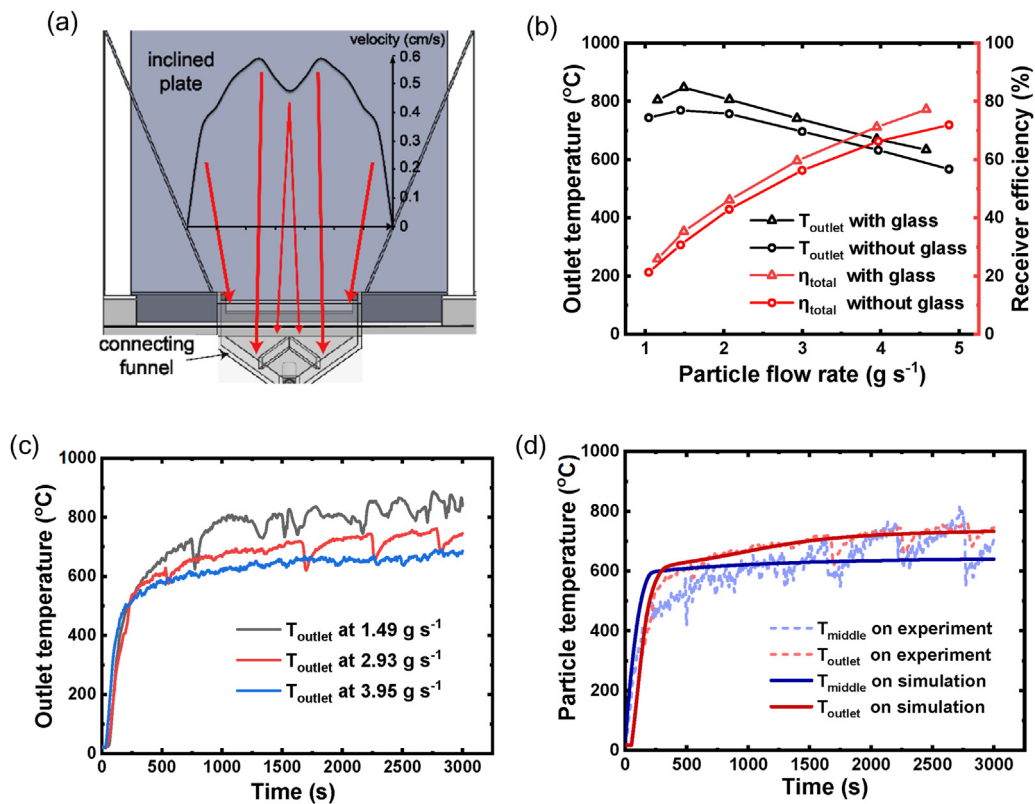


Fig. 7. (a) Velocity distribution of particles on the surface of flowing particle layer, (b)  $T_{outlet}$  and  $\eta_{total}$  at various particle flow rates with and without quartz glass on aperture, (c) real-time  $T_{outlet}$  at various flow rates, and (d) real-time  $T_{middle}$  and  $T_{outlet}$  at 2.93 g/s on experiment and simulation with quartz glass on aperture.

#### 4.2. Numerical studies

Figs. 7(d) and Fig. 8(a) helped develop and validate the model, where good agreements were achieved between the experimental data and simulation results. Compared with the experimental method, numerical simulation can provide a more comprehensive understanding of the operating characteristics of the sliding-bed receiver, such as the endothermic process of particles and the composition of the energy loss.

The simulated flowing particle temperature ( $T_{fp}$ ) and average incident power ( $Q_{rad,inc}$ ) along the particle path is presented in Fig. 8(b). Three cases of small (1.158 g/s), medium (1.492 g/s) and large (2.074 g/s) flow rate were detailedly compared. With the increase of particle flow rate from 1.158 g/s to 2.074 g/s, the peak temperature was reduced by 87 °C, but the particle temperature

difference at the end of the inclined plate was only 37 °C. The decrease of temperature difference from 87 °C to 37 °C was due to the longer temperature drop section at small flow rate (70 mm) than that at large flow rate (20 mm). The so-called temperature drop could be explained through the endothermic process of particles along the path. As the particles flow downward, the incident radiation increased first and then decreased. During the increase of the incident radiation, the particle temperature was always lower than the equilibrium temperature corresponding to the incident radiation, thus keeping increasing. While during the decrease of the incident radiation, the particle temperature could finally exceed the equilibrium temperature corresponding to the incident radiation, i.e. the heat dissipation of high-temperature particles could finally exceed the incident radiation, leading to the temperature drop. Considering the comparison between the cases of small and

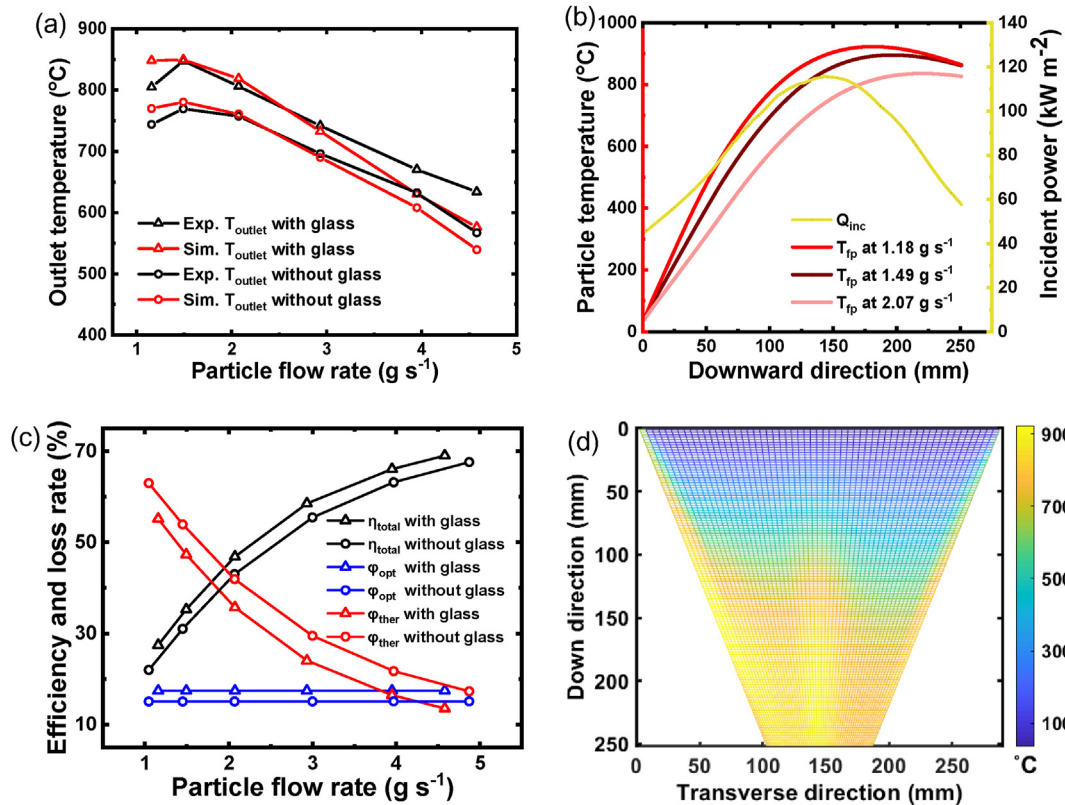


Fig. 8. (a) Comparison between experimental and simulated results, (b)  $Q_{rad,inc}$  and simulated  $T_{fp}$  along the inclined plate with quartz glass, (c) Simulated  $\eta_{total}$ ,  $\phi_{opt}$  and  $\phi_{ther}$  vs.  $\dot{m}_{sum}$ , (d) Simulated temperature distribution of  $T_{fp}$  on the inclined plate at 2.07 g/s with quartz glass.

medium flow rate, the small flow rate case had a slightly higher particle temperature at the end of the inclined plate, but also had longer residence time which led to a larger thermal loss in the connecting funnel. Therefore, too small flow rate would not only lead to a lower efficiency, but also would lead to a lower outlet temperature, which matched the change trend as presented in Fig. 8(a). Temperature drop section was a waste of incident power, and not conducive to higher efficiency. The above analysis could help optimize the design and operation of this sliding-bed particle receiver and other types of particle receiver such as free-falling particle receivers. A few simple guidelines were given below. 1) reducing the temperature drop section by adjusting the distribution of particle velocity and incident power would improve the receiver efficiency; 2) A better particle flow rate should be at least higher than the turning point as shown in Fig. 7(b); 3) The ideal incident power distribution should be that the incident power increased along the particle flow direction. Furthermore, the significance of guideline 1 and the controllability of velocity distribution could be understood as follows. The particles on different streamlines might have different endothermic processes, and the control of velocity distribution could optimize the management of temperature drop sections for different streamlines in more detail. A simple example is that in order to match the incident light spot with high middle radiation intensity and low edge radiation intensity, the particles in the middle streamline should be faster than the particles in the edge, which can effectively improve the outlet particle temperature and the efficiency of the receiver.

The total efficiency ( $\eta_{total}$ ), the optical loss rate ( $\phi_{opt}$ ) and the thermal loss rate ( $\phi_{ther}$ ) were further simulated as presented in Fig. 8(c). Quartz glass was found to reduce  $\phi_{ther}$  by more than 5% due to the greenhouse effect, but also increased the  $\phi_{opt}$  by about 2.4% due to the reflection of incident rays. As a result, the quartz

glass on aperture improved  $\eta_{total}$  by 3%–4% in experimental cases.

The particle temperature distribution on inclined plate is presented in Fig. 8(d). The distribution characteristic was mainly determined by the distribution of incident power and particle velocity, where the highest temperature areas were always found to be related with a high incident power and a low particle velocity. For the particles at the edge of flow, despite the weaker radiation, a high temperature would still be reached due to the lower particle velocity as shown in Fig. 8(d), which indicated the risk of overheating. Extra attention should be given to avoid slow flow areas, especially with a higher incident power.

### 4.3. Model forecast

In practical applications such as the dish-type (0.01–0.4 MWe) and the tower-type (10–150MWe) concentrated solar power systems [22], the incident power is much larger than the solar simulator as tested in previous section. Therefore, numerical studies to further improve  $T_{outlet}$  and  $\eta_{total}$  were conducted considering a much higher incident power in this section.

The characteristics of  $T_{outlet}$  and  $\eta_{total}$  at various  $Q_{rad,inc}$  (4 kW–100 MW) without quartz glass were presented in Fig. 9(a). With the increase of  $Q_{rad,inc}$ , higher  $T_{outlet}$  and  $\eta_{total}$  could be achieved. When  $Q_{rad,inc}$  reached 1 MW,  $T_{outlet}$  could reach 1350 °C and 750 °C at 0.5 kg/s and 1 kg/s particle flow rate, respectively.

The influence of quartz glass on the sliding-bed receiver performance was analyzed in detail through the study of the characteristics of  $\phi_{opt}$  and  $\phi_{ther}$  under various incident conditions (4 kW–100 MW). As shown in Fig. 9(b), a continuous decrease of  $\phi_{ther}$  and a relative stability of  $\phi_{opt}$  were observed with the increase of incident power. With the increase of incident power, the particle flow rate should also be increased to avoid the overheating of

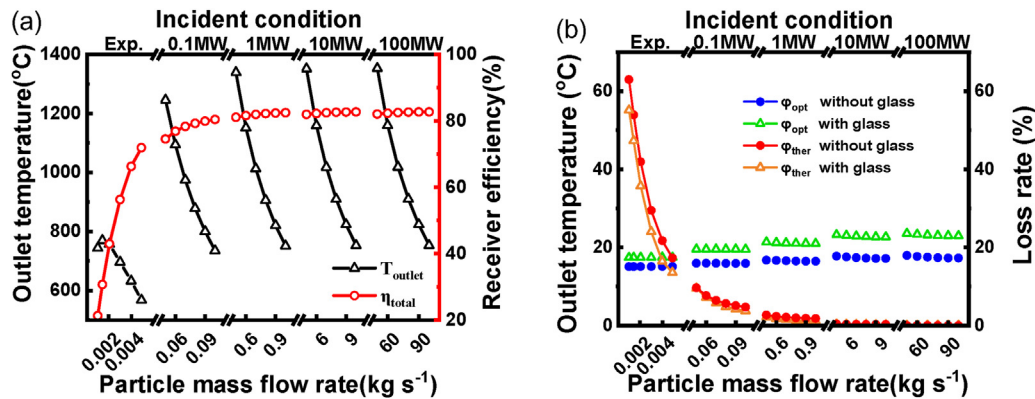


Fig. 9. (a)  $T_{outlet}$  and  $\eta_{total}$  vs.  $\dot{m}_{sum}$ , and (b)  $T_{outlet}$ ,  $\varphi_{opt}$  and  $\varphi_{ther}$  with and without quartz glass under the real experimental, simulated dish-type and tower-type concentrating condition.

particles. Therefore, the thermal loss (i.e. the conduction, convection and radiation losses) directly related to temperature did not increase proportionally with the incident power, which caused the decrease of  $\varphi_{ther}$ . Different from thermal loss, optical loss almost increased proportionally with the incident power due to the relatively constant reflectivity of particles and quartz glass, which caused the relative stability of  $\varphi_{opt}$ . As a result, quartz glass was found to be unfavorable for the large  $Q_{rad,inc}$  conditions ( $>0.1$  MW), when  $\varphi_{opt}$  became far more important than  $\varphi_{ther}$ . However, quartz glass was still necessary for stable operation of particle receivers in windy and rainy weather.

## 5. Conclusions

A novel impeded flow particle receiver, which was named as a sliding-bed particle receiver, was proposed to solve the problems of thermal deterioration risk and real-time particle velocity control difficulty for the previous impeded flow particle receivers and further have the potential to achieve the particle velocity distribution control to match the non-uniformity of incident power. The sliding-bed receiver's structural validity and operational characteristics at different working conditions were detailedly investigated with both experimental and numerical methods. A high outlet temperature reaching  $847^{\circ}\text{C}$  and a high efficiency reaching 77.2% were observed under a solar simulator of 4 kW. The quartz glass on aperture was found to help improve the receiver performance with greenhouse effect. The sliding-bed receiver was found to have a quick start for that particles inside could be heating to over 80% of the final stable temperature within 10 min. An optical and thermal coupling model was developed to provide a more comprehensive understanding of the operating characteristics of the sliding-bed receiver. Analysis based on experiment and simulation revealed the effects of the effects of the incident power distribution, the particle velocity distribution and the quartz glass on aperture on the performance of this receiver, which could help optimize the design and operation of the sliding-bed particle receiver and other particle receivers such as free-falling particle receivers. Numerical models further revealed an improved particle temperature of  $1350^{\circ}\text{C}$  and efficiency of 82% in practical applications such as the dish-type (0.01–0.4 MWe) and the tower-type (10–150MWe) concentrated solar power systems, when the quartz glass might have negative effect on efficiency improvement. In addition, a larger receiver with multiple outlet valves and secondary reflection technology is in manufacturing, trying to achieve the real-time velocity distribution control and higher operating parameters in a real tower-type concentrated solar power system of  $\sim 500$  kW.

## CRediT authorship contribution statement

**Xiangyu Xie:** Conceptualization, Methodology, Software, Investigation, Formal analysis, Writing – original draft, Visualization. **Haoran Xu:** Validation, Formal analysis, Writing – review & editing. **Di Gan:** Investigation, Formal analysis. **Mingjiang Ni:** Supervision. **Jianhua Yan:** Supervision. **Kefa Cen:** Supervision. **Gang Xiao:** Conceptualization, Methodology, Writing – review & editing, Supervision.

## Declaration of competing interest

The authors declare that they have no known competing financial interests or personal relationships that could have appeared to influence the work reported in this paper.

## Acknowledgements

The authors gratefully acknowledge the support from the Zhejiang Provincial Natural Science Foundation (NO. LR20E060001) and the National Natural Science Foundation of China (No. 51776186).

## References

- [1] K. Jiang, X. Du, Y. Kong, C. Xu, X. Ju, A comprehensive review on solid particle receivers of concentrated solar power, *Renew. Sustain. Energy Rev.* 116 (2019) 109463.
- [2] C.K. Ho, A review of high-temperature particle receivers for concentrating solar power, *Appl. Therm. Eng.* 109 (2016) 958–969.
- [4] T. Baumann, S. Zunft, Properties of granular materials as heat transfer and storage medium in CSP application, *Sol. Energy Mater. Sol. Cells.* 143 (2015) 38–47.
- [5] Q. Kang, G. Flamant, R. Dewil, J. Baeyens, H.L. Zhang, Y.M. Deng, Particles in a circulation loop for solar energy capture and storage, *Particuology* 43 (2019) 149–156.
- [6] T. Tan, Y. Chen, Review of study on solid particle solar receivers, *Renew. Sustain. Energy Rev.* 14 (2010) 265–276.
- [7] G. Xiao, K. Guo, Z. Luo, M. Ni, Y. Zhang, C. Wang, Simulation and experimental study on a spiral solid particle solar receiver, *Appl. Energy* 113 (2014) 178–188.
- [8] J.M. Hruby, B.R. Steele, Solid particle central receiver for solar energy, *Chem. Eng. Prog.* 82 (1986) 44–47.
- [9] C.K. Ho, J. Christian, J. Yellowhair, S. Jeter, M. Golob, C. Nguyen, et al., Highlights of the high-temperature falling particle receiver project: 2012 - 2016, *AIP Conf Proc* 1850 (2017).
- [10] C.K. Ho, J.M. Christian, J. Yellowhair, N. Siegel, S. Jeter, M. Golob, et al., On-sun Testing of an Advanced Falling Particle Receiver System, vol. 1734, 2016, 030022.
- [11] C.K. Ho, C.K. Ho, J.M. Christian, J.E. Yellowhair, K. Armiijo, On-sun performance evaluation of alternative high-temperature falling particle receiver designs, *J. Sol. Energy Eng.* (2019) 141.
- [12] Taegyung Lee, Seungwon Shin, S.I. Abdel-Khalik, Parametric investigation of

- particulate flow in interconnected porous media for central particle-heating receiver, *J. Mech. Sci. Technol.* 32 (3) (2018) 1181–1186.
- [13] M. Sandlin, S.I. Abdel-Khalik, A study of granular flow through horizontal wire mesh screens for concentrated solar power particle heating receiver applications – Part II: parametric model predictions, *Sol. Energy* 174 (2018) 1252–1262.
- [14] M. Sandlin, S.I. Abdel-Khalik, A study of granular flow through horizontal wire mesh screens for concentrated solar power particle heating receiver applications – Part I: experimental studies and numerical model development, *Sol. Energy* 169 (2018) 1–10.
- [15] C.K. Ho, G. Peacock, J.M. Christian, K. Albrecht, J.E. Yellowhair, D. Ray, On-sun Testing of a 1 MWt Particle Receiver with Automated Particle Mass-Flow and Temperature Control, vol. 2126, 2019, 030027.
- [16] W. Wu, L. Amsbeck, R. Buck, R. Uhlig, R. Ritz-Paal, Proof of concept test of a centrifugal particle receiver, *Energy Procedia* 49 (2014) 560–568.
- [17] W. Wu, D. Trebing, L. Amsbeck, R. Buck, Prototype testing of a centrifugal particle receiver for high-temperature concentrating solar applications, *J. Sol. Energy Eng.* 137 (2015).
- [18] M. Ebert, L. Amsbeck, J. Rheinländer, B. Schlögl-Knothe, S. Schmitz, M. Sibum, et al., Operational Experience of a Centrifugal Particle Receiver Prototype, vol. 2126, 2019, 030018.
- [19] G. Xiao, K. Guo, M. Ni, Z. Luo, K. Cen, Optical and thermal performance of a high-temperature spiral solar particle receiver, *Sol. Energy* 109 (2014) 200–213.
- [20] J. Ballestrín, C.A. Estrada, M. Rodríguez-Alonso, C. Pérez-Rábago, L.W. Langley, A. Barnes, Heat flux sensors: calorimeters or radiometers? *Sol. Energy* 80 (2006) 1314–1320.
- [21] S. Ulmer, W. Reinalter, P. Heller, E. Lüpfert, D. Martínez, Beam characterization and improvement with a flux mapping system for dish concentrators, *J. Sol. Energy Eng.* 124 (2002) 182–188.
- [22] M.T. Islam, N. Huda, A.B. Abdullah, R. Saidur, A comprehensive review of state-of-the-art concentrating solar power (CSP) technologies: current status and research trends, *Renew. Sustain. Energy Rev.* 91 (2018) 987–1018.